

# Slowly rotating $\mathcal{C}$ -stars

Philip Beltracchi\*

Camilo Posada†

*Research Centre for Theoretical Physics and Astrophysics, Institute of Physics,  
Silesian University in Opava, Bezručovo nám. 13, CZ-746 01 Opava, Czech Republic and  
Programa de Matemática, Fundación Universitaria Konrad Lorenz, 110231 Bogotá, Colombia*

The equilibrium configurations of slowly rotating anisotropic self-gravitating fluids are computed using the extended Hartle structure equations, including anisotropic effects, derived in our previous paper. We focus on the so-called  $\mathcal{C}$ -star, whose anisotropic pressure follows a fully covariant equation of state (EoS), while a standard polytrope describes the radial pressure. We determine surface and integral properties, such as the moment of inertia, mass change, mass quadrupole moment, and ellipticity. Notably, for certain values of the compactness parameter, highly anisotropic  $\mathcal{C}$ -stars exhibit a prolate shape rather than the typical oblate form — an intriguing behavior also observed in other anisotropic systems like Bowers-Liang spheres and stars governed by a quasi-local EoS. Although the  $\mathcal{C}$ -stars considered in this study are limited by stability criteria and cannot sustain compactness beyond  $M/R \approx 0.38$ , we found indications that certain rotational perturbations exhibit similarities to those observed in other ultracompact systems approaching the black hole limit.

## I. INTRODUCTION

In a recent paper [1], we extended Hartle’s second-order framework in angular frequency for slowly rotating relativistic stars [2, 3] to incorporate anisotropic configurations within general relativity. Various approaches have been developed to study rotating systems in general relativity, each with its own advantages and limitations. For instance, the Newman-Janis algorithm [4–6], which was instrumental in the discovery of the Kerr-Newman metric, has been generalized in several ways [7–9] to generate rotating versions of spherically symmetric spacetimes. While these extensions of the Newman-Janis algorithm provide exact solutions to the Einstein field equations, they generally do not preserve the EoS between the static and rotating configurations [10, 11].

Additionally, several perturbative approaches have been developed to model slowly rotating systems. The Lense-Thirring metric describes frame-dragging effects in weak gravitational fields [12], while the Hartle-Thorne [2, 3] method extends this framework to study the second-order in rotation structural changes in rotating objects obeying a perfect fluid EoS. Our work further generalizes this formalism to include systems with more general EoSs [1]. As an application of this formalism, we examined the structure and integral properties of slowly rotating Bowers-Liang spheres [1], which are characterized by uniform density and anisotropic pressure. While the Bowers-Liang sphere provides a simple, closed-form analytic solution, its physical relevance is limited by the assumption of constant density and the *ad hoc* nature of its anisotropic EoS.

Although neutron stars (NSs) are usually modeled with isotropic pressure, it has been proposed that various physical phenomena can lead to local anisotropies; for instance, strong magnetic fields [13–15], pion condensation [16], scalar fields minimally coupled to gravity [17], among others [18]. The effect of anisotropy on the NSs properties has been studied in a number of papers [19–24]. In this context, several methods to introduce anisotropies have been proposed in the literature. Cosenza *et al.* [25] proposed an anisotropic term proportional to the gravitational force. A quasi-local EoS for the anisotropic pressures, where the anisotropy is proportional to the compactness and the radial pressure, was proposed by [26]. Additional methods include the complexity factor approach [27], the minimal geometric deformation [28], and the covariant method proposed by [29]. More recently, [30, 31] proposed relativistic elastic stars as possible models of ultracompact objects and BH mimickers.

Among the various methods discussed above for introducing anisotropies, the covariant approach proposed by [29], or  $\mathcal{C}$ -star, offers a viable alternative for obtaining a rotating solution while preserving the EoS. In this model, the anisotropy is proportional to the directional derivative of the pressure, a certain arbitrary function of the mass density, and a parameter  $\mathcal{C}$  that quantifies the ‘strength’ of the anisotropy. For specific parameter choices of the solution, [29] found that  $\mathcal{C}$ -stars are stable, have vanishing tidal Love numbers, and produce gravitational wave echoes when perturbed.

In this paper, we employ the extended Hartle structure equations derived in [1] (see also [32]), to study the structure and integral properties of slowly rotating  $\mathcal{C}$ -stars, up to second order in angular velocity. We consider a  $\mathcal{C}$ -star model in which the anisotropic EoS follows the covariant approach outlined above, while the EoS relating radial pressure to mass density corresponds to a standard poly-

\* phipbel@aol.com

† camoposada82@gmail.com

trope. Thus, our analysis extends the work of Ref. [33] on slowly rotating isotropic polytropes.

Recently, [34] reported a short study of  $\mathcal{C}$ -stars in slow rotation. However, they restricted their analysis to investigating the impact of the anisotropy on the mass, radius, binding energy, and moment of inertia. Our analysis complements and extends the one in [34] in several ways: first of all, we compute all the monopole and quadrupole perturbation functions for  $\mathcal{C}$ -stars, up to order  $\Omega^2$ . We also determine the surface and integral properties, such as the moment of inertia, the change of mass, the ellipticity, and the mass quadrupole moment.

The structure of the paper is as follows. In Sec. II we review the extended formalism for slowly rotating anisotropic relativistic stars. In Sec. III we summarize the covariant model for anisotropic relativistic fluids, or  $\mathcal{C}$ -stars. The rotational properties, as well as structure and integral properties of  $\mathcal{C}$ -stars are presented in Sec. IV. Finally, in Sec. V we discuss our final conclusions and open questions for future work.

## II. REVIEW OF THE SLOWLY ROTATING ANISOTROPIC HARTLE FORMALISM

The structure equations for slowly rotating anisotropic configurations were already derived in [1], therefore, we refer the reader to that reference for further details. Here, we summarize the formalism and main results.

### A. Rotational metric perturbations and energy-momentum tensor are specified

The standard Hartle perturbative metric for slowly rotating systems reads [2, 3]

$$ds^2 = -e^{2\nu_0(r)} \left[ 1 + 2h_0(r) + 2h_2(r) P_2(\cos\theta) \right] dt^2 + e^{2\lambda_0(r)} \left\{ 1 + \frac{2e^{2\lambda_0(r)}}{r} \left[ m_0(r) + m_2(r) P_2(\cos\theta) \right] \right\} dr^2 + r^2 \left[ 1 + 2k_2(r) P_2(\cos\theta) \right] \left[ d\theta^2 + \sin^2\theta (d\phi - \omega(r)dt)^2 \right]. \quad (1)$$

Here,  $P_l(\cos\theta)$  is the Legendre polynomial of order  $l$ ,  $\nu_0(r)$  and  $\lambda_0(r)$  are the metric functions of the non-rotating solution, and  $h_l(r)$ ,  $k_l(r)$ , and  $m_l(r)$ , are the monopole ( $l=0$ ) and quadrupole ( $l=2$ ) perturbations of order  $\Omega^2$  in rotation, respectively. The function  $\omega(r)$  is the contribution at the first-order in  $\Omega$ , which gives rise to the inertial frame dragging. The condition  $k_0(r) = 0$  corresponds to Hartle's choice of gauge [2].

One convenient way to write the energy-momentum tensor (EMT) for a rotating anisotropic configuration is

$$T^\mu_\nu = (\mathcal{E} + \mathcal{T})u^\mu u_\nu + \mathcal{T}\delta^\mu_\nu - (\mathcal{T} - \mathcal{P})v^\mu v_\nu, \quad (2)$$

where  $\mathcal{T}$  is the transverse pressure in the comoving frame of the rotating fluid,  $\mathcal{P}$  is the radial pressure,  $\mathcal{E}$  is the

energy density,  $u$  is a normalized four-velocity, and  $v$  is a normalized vector along the spacelike eigenvector with a distinct eigenvalue. The eigenvalues of the EMT are  $\mathcal{E}$ ,  $\mathcal{P}$ , and  $\mathcal{T}$  twice, so this is still Segre type [(11)1,1]. We can similarly expand the eigenvalues to Hartle [2],

$$\mathcal{E} = \rho(r) + \mathcal{E}_0(r) + \mathcal{E}_2(r)P_2(\cos\theta), \quad (3)$$

$$\mathcal{P} = p_r(r) + \mathcal{P}_0(r) + \mathcal{P}_2(r)P_2(\cos\theta), \quad (4)$$

$$\mathcal{T} = p_\perp(r) + \mathcal{T}_0(r) + \mathcal{T}_2(r)P_2(\cos\theta), \quad (5)$$

where we have zeroth-order terms and second-order monopole and quadrupole terms in rotation.

For the four-vectors in Eq. (2) we use the same four-velocity as the standard Hartle formalism

$$u^t = (-g_{tt} - 2\Omega g_{t\phi} - \Omega^2 g_{\phi\phi})^{-1/2}, \\ u^\phi = \Omega u^t, \quad u^r = u^\theta = 0, \quad (6)$$

and [1]

$$v^\mu = \left( 0, \frac{1}{\sqrt{g_{rr}}}, Y\Omega^2, 0 \right), \quad (7)$$

with

$$(p_r - p_\perp)Y = \Upsilon(r) \sin\theta \cos\theta, \quad (8)$$

in  $(t, r, \theta, \phi)$  coordinates.

### B. A non-rotating configuration is computed

To the zeroth order in  $\Omega$ , we recover a spherically symmetric line element in the standard Schwarzschild form

$$ds^2 = -e^{2\nu(r)} dt^2 + e^{2\lambda(r)} dr^2 + r^2 (d\theta^2 + \sin^2\theta d\phi^2), \quad (9)$$

where  $\nu$  and  $\lambda$  are functions of the radial coordinate  $r$ , only. Thus, a locally anisotropic EMT takes the general form

$$T^\mu_\nu = \text{diag}(-\rho, p_r, p_\perp, p_\perp), \quad (10)$$

where  $\rho$  is the energy density, and  $p_\perp = p_\theta = p_\phi$ .

For a given value of the central density, the non-rotating solution is determined by integrating the Anisotropic Tolman-Oppenheimer-Volkoff (ATOV) equation of hydrostatic equilibrium for the radial pressure  $p_r$  [1]

$$\frac{dp_r}{dr} = -(\rho + p_r) \frac{(m + 4\pi r^3 p_r)}{r(r - 2m)} + \frac{2}{r}(p_\perp - p_r), \quad (11)$$

and the equation for the total mass  $m(r)$  enclosed inside a spherical surface of radius  $r$

$$\frac{dm}{dr} = 4\pi\rho(r)r^2. \quad (12)$$

The mass  $m(r)$  is connected to the  $g_{rr}$  metric component, via the standard relation

$$e^{-2\lambda} = 1 - \frac{2m(r)}{r}. \quad (13)$$

In the isotropic case, where  $p_{\perp} = p_r$ , Eq. (11) reduces to the standard TOV equation.

The system (11)-(13) consists of three equations with five unknowns, requiring two additional EoSs to relate  $\rho$ ,  $p_r$ , and  $p_{\perp}$ . Once the EoSs are specified, the integration is performed from the center of the star with the initial conditions  $m(0) = 0$ ,  $\rho(0) = \rho_c$  (where  $\rho_c$  is the central density), and  $p(\rho_c) = p_c$ , where the central pressure  $p_c$  is given by the corresponding EoS. The radius of the configuration is determined by imposing the boundary condition  $p_r(R) = 0$ , where  $R$  denotes the stellar surface.

The remaining metric function  $\nu(r)$  can be obtained by integrating outward from the origin the equation

$$\frac{d\nu}{dr} = \frac{(m + 4\pi r^3 p_r)}{r(r - 2m)}, \quad (14)$$

with the boundary condition  $e^{2\nu(R)} = 1 - 2M/R$ , from the matching at the boundary with the exterior Schwarzschild solution.

### 1. Exterior spacetime and matching conditions

In the exterior vacuum spacetime  $\rho = p = 0$ , thus the spacetime geometry is described by Schwarzschild's exterior solution

$$e^{2\nu(r)} = e^{-2\lambda(r)} = 1 - \frac{2M}{r}, \quad r > R. \quad (15)$$

Unless there is a junction layer at the surface, the interior and exterior geometries are matched at the boundary  $\Sigma = R$ , such that

$$[\nu] = 0, \quad [\nu'] = 0, \quad [\lambda] = 0, \quad (16)$$

where the prime denotes derivative with respect to the  $r$  coordinate, and  $[f]$  indicates the difference between the value of  $f$  in the vacuum exterior and its value in the interior, evaluated at  $\Sigma$ , i.e.,  $[f] = f^+|_{\Sigma} - f^-|_{\Sigma}$ .

### C. Frame dragging and moment of inertia

The  $t\phi$ , or  $\phi t$ , components of the Einstein equations are first order in  $\Omega$ . Defining the functions

$$\varpi \equiv \Omega - \omega, \quad (17)$$

and

$$j \equiv e^{-(\nu_0 + \lambda_0)} = e^{-\nu_0} \sqrt{1 - \frac{2m}{r}}, \quad (18)$$

the frame-dragging equation can be written as [1] (see also [35]).

$$\frac{1}{r^4} \frac{d}{dr} \left( r^4 j \frac{d\varpi}{dr} \right) + \frac{4j' \varpi}{r} \frac{\rho + p_{\perp}}{\rho + p_r} = 0. \quad (19)$$

In the isotropic case, where  $p_r = p_{\perp}$ , Eq. (19) reduces to the original Hartle relation [2].

In the exterior region  $r > R$ ,  $\epsilon = p = 0$  and  $j(r) = 1$ , thus Eq. (19) can be solved explicitly to give

$$\varpi(r)^+ = \Omega - \frac{2J}{r^3}, \quad (20)$$

where  $J$  is an integration constant associated with the angular momentum of the star [2]. For the interior solution, Eq. (19) is integrated outward from the origin with the boundary conditions

$$\varpi(0) = \varpi_c = \text{const.}, \quad (21a)$$

$$\left( \frac{d\varpi}{dr} \right)_{r=0} = 0. \quad (21b)$$

Regularity of the solution at the surface demands that  $[\varpi] = [\varpi'] = 0$ . Thus, one integrates numerically Eq. (19) and obtains the surface value  $\varpi(R)$ . Then, and only then, one can determine the angular momentum  $J$  and the angular velocity  $\Omega$  as

$$J = \frac{1}{6} R^4 \left( \frac{d\varpi}{dr} \right)_{r=R}, \quad \Omega = \varpi(R) + \frac{2J}{R^3}. \quad (22)$$

Once the angular momentum and angular velocity are determined, the relativistic moment of inertia can be obtained from the relation  $I = J/\Omega$ .

### D. The monopole perturbations: the $l = 0$ sector

There are three differential equations for the monopole sector. The one for the perturbation function  $m_0$  comes from the  $tt$  component of Einstein's equation [1]

$$\frac{dm_0}{dr} = 4\pi r^2 \mathcal{E}_0 + \frac{j^2 r^4}{12} \left( \frac{d\varpi}{dr} \right)^2 - \frac{r^3 \varpi^2}{3} \frac{dj^2}{dr} \frac{\rho + p_{\perp}}{\rho + p_r}. \quad (23)$$

The  $rr$  perturbation equation gives a differential equation for  $h_0$  in the form [1]

$$\frac{dh_0}{dr} = 4\pi r e^{2\lambda} \mathcal{P}_0 + \frac{(1 + 8\pi r^2 p_r)}{(r - 2m)^2} m_0 - \frac{e^{2\lambda} r^3 j^2 \varpi'^2}{12}. \quad (24)$$

Finally, we use  $(8\pi T_{\theta}^{\theta} - G_{\theta}^{\theta}) + (8\pi T_{\phi}^{\phi} - G_{\phi}^{\phi}) = 0$ , or the monopole perturbation to the  $r$  component of the EMT conservation  $\nabla_{\mu} T^{\mu}_{\nu} = 0$ , to derive [1]

$$\begin{aligned} \frac{d\mathcal{P}_0}{dr} = & -(\mathcal{E}_0 + \mathcal{P}_0) \nu'_0 + \frac{2(\mathcal{T}_0 - \mathcal{P}_0)}{r} + \frac{\rho + p_{\perp}}{3} \frac{d}{dr} \left( \frac{r^3 \varpi^2 j^2}{r - 2m} \right) \\ & + \frac{(\rho + p_r)}{r - 2m} \left[ \frac{r^4 j^2 \varpi'^2}{12} - 4\pi r^2 \mathcal{P}_0 - \frac{(1 + 8\pi r^2 p_r)}{(r - 2m)} m_0 \right]. \end{aligned} \quad (25)$$

These equations are integrated outward, from the origin, where  $m_0(0) = \mathcal{P}_0(0) = 0$ .

### 1. Matching and setup for the monopole sector

We find it convenient to define the auxiliary function

$$H_0 \equiv h_0 - h_c, \quad (26)$$

where  $h_c$  is a constant to be determined. We recognize that  $H_0$  also follows the differential equation (24), thus it can be integrated with the initial condition  $H_0(0) = 0$ . We then find the corresponding value of  $h_c$  by continuity, and the values of  $H_0(r \rightarrow R^-)$  and the exterior  $h_0(r \rightarrow R^+)$ , since the background  $g_{tt}$  is nonzero in this case.

In the vacuum exterior where  $\rho = p = 0$ , Eqs. (23) and (24) can be integrated explicitly giving

$$m_0^+ = \delta M - \frac{J^2}{r^3}, \quad (27)$$

$$h_0^+ = -\frac{m_0}{r - 2M}, \quad (28)$$

where  $\delta M$  is a constant of integration associated with the change of mass induced by the rotation.

In his approach, Hartle [2] assumed the continuity of  $m_0$  and  $h_0$ , at the surface, i.e.,  $[h_0] = [m_0] = 0$ . This condition was employed to determine the constant  $\delta M$ . In [36], it was argued that for systems where the density at the surface is nonzero, a discontinuity appears in  $m_0$ , thus providing an extra term in (27). In the anisotropic case, it can be shown that the modified change of mass takes the general form [1]

$$\delta M_{\text{mod}} = m_0(R) + \frac{J^2}{R^3} + 4\pi\rho(R)R^2\xi_0, \quad (29)$$

where  $\xi_0$  is the spherical deformation parameter

$$\xi_0 = -\frac{\mathcal{P}_0}{p'_r(r \rightarrow R^-)}. \quad (30)$$

A derivation of Eq. (29) is presented in [1]. However, this extra term is unnecessary in our case since the EoSs we consider guarantee that the density vanishes at the surface.

### E. The quadrupole perturbations: the $l = 2$ sector

The quadrupole sector is dependent on the three-metric perturbation functions  $h_2, k_2, m_2$ , three EMT eigenvalue perturbation functions  $\mathcal{E}_2, \mathcal{P}_2, \mathcal{T}_2$ , and an EMT eigenvector perturbation function  $\Upsilon$  for a total of seven functions (in contrast to five in the isotropic case) [1]. One equation comes from the Einstein equations  $r\theta$  component

$$8\pi r^3 \Upsilon(r) = 3e^{-\lambda} \left[ r \frac{d}{dr} (h_2 + k_2) + h_2 \left( r \frac{d\nu_0}{dr} - 1 \right) - \frac{m_2}{r - 2m} \left( r \frac{d\nu_0}{dr} + 1 \right) \right]. \quad (31)$$

Additionally, the  $\theta$  component of the EMT conservation equation gives

$$3\mathcal{T}_2 + (\rho + p_\perp) (3h_2 + e^{-2\nu_0} \varpi^2 r^2) = (p_r - p_\perp) \left( \frac{3e^{2\lambda}}{r} \right) m_2 + e^{-\lambda} [r\Upsilon(4 + r\nu'_0) + r^2\Upsilon']. \quad (32)$$

Using the difference between the  $\theta\theta$  and  $\phi\phi$  components  $(8\pi T^\theta_\theta - G^\theta_\theta) - (8\pi T^\phi_\phi - G^\phi_\phi) = 0$ , we obtain a fairly simple equation which could eliminate  $m_2$  or  $h_2$

$$m_2 = (r - 2m) \left[ \frac{j^2 r^4 \varpi'^2}{6} - \frac{r^3 \varpi^2}{3} \left( \frac{dj^2}{dr} \right) \frac{\rho + p_\perp}{\rho + p_r} - h_2 \right]. \quad (33)$$

Using Eq. (33) to replace  $m_2$ , the  $rr$  component of the Einstein field equations can be written as

$$\frac{j^2 r^2}{3} \left[ 16\pi(\rho + p_\perp)(1 + 2r\nu'_0)\varpi^2 + \left( \frac{3}{2} + 8\pi r^2 p_r \right) \left( \frac{d\varpi}{dr} \right)^2 \right] = -8\pi\mathcal{P}_2 + \frac{2(r - 2m)}{r^2} \left[ \frac{dh_2}{dr} + (1 + r\nu'_0) \frac{dk_2}{dr} \right] + \frac{4}{r^2} [h_2(4\pi r^2 p_r - 1) - k_2]. \quad (34)$$

Finally, the quadrupole perturbation to the  $r$  compo-

nent of  $\nabla_\mu T^\mu_\nu = 0$  gives the following equation

$$\begin{aligned} \frac{d\mathcal{P}_2}{dr} = & \frac{2(\mathcal{T}_2 - \mathcal{P}_2)}{r} - (\mathcal{E}_2 + \mathcal{P}_2)\nu'_0 + \frac{2}{3}r\varpi e^{-2\nu_0}(\rho + p_\perp) \left[ 2\varpi(1 + 2r\nu'_0) - r \left( \frac{d\varpi}{dr} \right) \right] + \frac{j^2 r(1 + r\nu'_0)}{8\pi} \left( \frac{d\varpi}{dr} \right)^2 \\ & - \left( \frac{3}{4\pi r^2} \right) \frac{d}{dr} (h_2 + k_2) - (\rho + p_r) \frac{dh_2}{dr} + 2(p_\perp - p_r) \frac{dk_2}{dr} - \left( \frac{3\nu'_0}{2\pi r^2} \right) h_2. \end{aligned} \quad (35)$$

The system of Eqs. (31)-(35), plus two EoSs defines the seven equations that determine the quadrupole sector.

### 1. Matching and setup for the quadrupole sector

In the vacuum exterior, the functions  $h_2$  and  $k_2$  are specified by [2, 3]

$$h_2 = \frac{J^2}{Mr^3} \left( 1 + \frac{M}{r} \right) + KQ_2^2(\zeta), \quad (36)$$

$$v_2 = h_2 + k_2 = -\frac{J^2}{r^4} + K \frac{2M}{[r(r-2M)]^{1/2}} Q_2^1(\zeta), \quad (37)$$

where  $K$  is a constant of integration, and  $Q_n^m$  are the associated Legendre functions of the second kind with argument  $\zeta \equiv (r/M) - 1$ , which read (following the convention in [2])

$$Q_2^1(\zeta) = \sqrt{\zeta^2 - 1} \left[ \frac{3\zeta^2 - 2}{\zeta^2 - 1} - \frac{3}{2}\zeta \log \left( \frac{\zeta + 1}{\zeta - 1} \right) \right], \quad (38a)$$

$$Q_2^2(\zeta) = \frac{3}{2} (\zeta^2 - 1) \log \left( \frac{\zeta + 1}{\zeta - 1} \right) - \frac{3\zeta^3 - 5\zeta}{\zeta^2 - 1}. \quad (38b)$$

In order to match with the exterior solution, one treats the interior equations by solving Eqs. (31)-(35) for both the particular case with nonzero  $\varpi$  and the homogeneous case with  $\varpi = 0$ , then choosing the true functions <sup>1</sup>

$$\text{true} = \text{particular} + A * \text{homogeneous}, \quad (39)$$

where  $A$  is the same constant for all the functions. The integration constants  $A$  and  $K$  can be determined by matching  $h_2$  and  $k_2$  to the exterior solutions given by Eqs. (36) and (37). Once the constant  $K$  has been determined, one can compute the mass quadrupole moment of the star, as measured at infinity, from the relation [3]

$$Q = \frac{J^2}{M} + \frac{8}{5} KM^3. \quad (40)$$

<sup>1</sup> Although [32] seems to have derived the same quadrupole equations, after our work [1] appeared, they do not describe the procedure of using the homogeneous solution to match the exterior solution at the outer boundary, which is crucial for solving the quadrupole sector.

Following the standard Hartle conventions [2], the EMT eigenvalue perturbations  $\mathcal{E}_2, \mathcal{P}_2, \mathcal{T}_2$  go to zero at the origin. The function  $\Upsilon$ , which describes the eigenvector perturbation, must go to zero at the origin for well-behaved systems because it is proportional to a factor of  $p_r - p_\perp$  which is zero there.

In addition to the behavior in the exterior, some constraints can be derived for the behavior near  $r = 0$ . For well behaved systems, the initial behavior of the relevant zeroth and first-order terms in  $\Omega$  are as follows

$$m = \frac{4\pi\rho_c}{3} r^3, \quad (41)$$

$$\nu_0 = \nu_c + \frac{2\pi}{3}(\rho_c + 3p_c)r^2, \quad (42)$$

$$p_r = p_\perp = p_c, \quad (43)$$

$$\rho = \rho_c, \quad (44)$$

$$\varpi = \varpi_c, \quad (45)$$

where the subscript ‘c’ denotes the value of the quantity at the center of the configuration. We can then find series solutions near the origin for the particular equations (31), (32), (34), and (35), as follows [1]

$$k_2^{(P)} = k_2^a r^2 + \dots + k_2^b r^4, \quad (46)$$

$$h_2^{(P)} = -k_2^a r^2 + \dots + h_2^b r^4, \quad (47)$$

The coefficients to the leading quadratic terms for the  $h_2$  and  $k_2$  metric functions must be equal and opposite. The lowest order terms in the  $\Upsilon, \mathcal{P}_2, \mathcal{T}_2$  functions are related to the quadratic and quartic, but not cubic <sup>2</sup>, coefficients of the  $h_2$  and  $k_2$  functions:

$$\Upsilon^{(P)} = \left[ \frac{3(h_2^b + k_2^b)}{2\pi} - e^{-2\nu_c} \varpi_c^2 (p_c + \rho_c) - k_2^a (3p_c + \rho_c) \right] r, \quad (48)$$

<sup>2</sup> The C-star exhibits cubic terms in the expansions of the quadrupole functions (see Eq. (88)), a feature absent in the Bowers-Liang sphere [1].

$$\mathcal{P}_2^{(P)} = \frac{1}{6} \left[ \frac{3(h_2^b + k_2^b)}{\pi} + 4k_2^a \rho_c - 4e^{-2\nu_c} \varpi_c^2 (p_c + \rho_c) \right] r^2, \quad (49)$$

$$\mathcal{T}_2^{(P)} = \left[ \frac{5(h_2^b + k_2^b)}{2\pi} - 2e^{-2\nu_c} \varpi_c^2 (p_c + \rho_c) - \frac{2}{3} k_2^a (6p_c + \rho_c) \right] r^2, \quad (50)$$

where  $h_2^b$ ,  $k_2^a$ , and  $k_2^b$  are arbitrary constants.

## 2. Deformation of the star

The rotational deformation of the star can be understood in the following way: A given constant  $p_r$  surface, lying at some radius  $r$  in the static configuration, upon rotation, is displaced to a radius

$$r + \xi_0(r) + \xi_2(r)P_2(\cos\theta), \quad (51)$$

where  $\xi_0$  is the monopole deformation given by (30), and the perturbation function  $\xi_2$  is defined as

$$\xi_2 = -\frac{\mathcal{P}_2}{p_r'(r \rightarrow R^-)}. \quad (52)$$

The ellipticity of the isobaric surfaces is given by [1]

$$\epsilon(r) = -\frac{3}{2r} [\xi_2(r) + rk_2(r)]. \quad (53)$$

The ellipticity of the stellar surface is computed by setting  $r = R$  in Eq. (53).

## III. C-STARS

We consider the covariant approach for anisotropic configurations proposed in [29], which introduces a covariant framework to satisfy the condition at the center,  $p_r = p_\perp$ . Although there is a certain degree of arbitrariness to fulfill this condition, [29] chose the following ansatz

$$p_\perp = p_r - \mathcal{C}f(\rho)v^\mu\nabla_\mu p_r, \quad (54)$$

where  $f(\rho)$  is a function of the density,  $v^\mu$  is the corresponding EMT eigenvector to  $p_r$ , and  $\mathcal{C}$  is a constant that quantifies the ‘strength’ of the anisotropy. Note that, by construction,  $p_r = p_\perp$  at the center for the static spherically symmetric case, since  $\partial_r p_r(0) = 0$ .

Considering the ansatz (54), the ATOV equation (11) takes the form

$$\frac{dp}{dr} = -\frac{(\rho + p_r)}{r(r-2m)} \frac{(m + 4\pi p_r r^3)}{1 + \frac{2}{r}\mathcal{C}f(\rho)\sqrt{1 - \frac{2m}{r}}}. \quad (55)$$

We recover the standard TOV equation in the isotropic case  $\mathcal{C} = 0$ . In order to close the system, we require two EoSs for  $p_r$  and  $f(\rho)$ . Following [29], we choose

$$f(\rho) = \rho, \quad (56)$$

which ensures the continuity of  $p_\perp$  and its derivative at the surface; for the radial pressure we choose a standard polytropic EoS

$$p_r = \kappa\rho_0^\gamma, \quad (57)$$

where  $\rho_0 = \rho - p_r/(\gamma - 1)$  denotes the rest-mass density,  $\kappa$  and  $\gamma = 1 + 1/n$  are constants for any particular model ( $n$  is the polytropic index). There are a few properties that led us to examine this EoS, or  $\mathcal{C}$ -star, for our rotating framework. First, it can be naturally expressed in terms of scalars, making it well-suited for generalization to the rotating case. In contrast, other promising methods in the spherically symmetric case, such as the quasi-local EoS [26], where the anisotropy is proportional to the compactness  $m(r)/r$ , is not formed from terms that we found an obvious way to isolate as scalars in the rotating case. Nevertheless, the quasi-local EoS has been extended to slow rotation [32] by writing the EoS, in the rotating case, in terms of the nonrotating compactness function. However, the authors in [32] did not elaborate on whether or not this is a valid approximation.

For this system, we can use the EoS to write the background equations (11) and (12) in terms of  $p_r$  and  $m$

$$\frac{dm}{dr} = 4\pi r^2 \left[ \frac{p_r}{\gamma - 1} + \left( \frac{p_r}{\kappa} \right)^{1/\gamma} \right], \quad (58)$$

$$\frac{dp_r}{dr} = -\frac{(m + 4\pi p_r r^3) \left[ (p_r/\kappa)^{1/\gamma} + (1+n)p_r \right]}{r(r-2m)} \times \left\{ 1 - \frac{2\mathcal{C}}{r} \left[ \left( \frac{p_r}{\kappa} \right)^{1/\gamma} + np_r \right] \sqrt{1 - \frac{2m}{r}} \right\}^{-1}, \quad (59)$$

or in terms of  $\rho_0$  and  $m$  as

$$\frac{dm}{dr} = 4\pi r^2 \left( \rho_0 + \frac{\kappa\rho_0^\gamma}{\gamma - 1} \right), \quad (60)$$

$$\frac{d\rho_0}{dr} = -\left( \frac{\rho_0^{-1/n}}{\gamma\kappa} \right) \times \frac{[\rho_0 + \kappa(1+n)\rho_0^\gamma] (m + 4\pi r^3 \kappa\rho_0^\gamma)}{r(r-2m) \left[ 1 + \frac{2\mathcal{C}}{r} \left( \rho_0 + \frac{\kappa\rho_0^\gamma}{\gamma-1} \right) \sqrt{1 - \frac{2m}{r}} \right]}. \quad (61)$$

In our approach, we consider the  $(\rho_0, m)$  representation because it gives the most stable numerical results.

### A. Equation of state and the perturbations

We carry out the generalization to the rotating case with  $\rho \rightarrow \mathcal{E}$ ,  $p_r \rightarrow \mathcal{P}$ , and  $p_\perp \rightarrow \mathcal{T}$ . Notice that since these are EMT eigenvalues, the covariant derivative term becomes the partial derivative  $\partial_\mu P$ .

It is possible to rewrite the EoSs (54), (56), and (57), purely in terms of  $\mathcal{P}$  and expand to get the expressions

$$\mathcal{E} = \left(\frac{\mathcal{P}}{\kappa}\right)^{1/\gamma} + \frac{\mathcal{P}}{\gamma-1}, \quad (62)$$

$$\mathcal{T} = \mathcal{P} - C \left[ \left(\frac{\mathcal{P}}{\kappa}\right)^{1/\gamma} + \frac{\mathcal{P}}{\gamma-1} \right] v^\mu \partial_\mu \mathcal{P}, \quad (63)$$

then,

$$\mathcal{E}_x = \left(\frac{d\mathcal{E}}{d\mathcal{P}}\right) \mathcal{P}_x = \left[ \frac{(\frac{p_r}{\kappa})^{1/\gamma}}{\gamma p_r} + \frac{1}{\gamma-1} \right] \mathcal{P}_x, \quad (64)$$

where the subscript  $x$  takes the values 0, 2, corresponding to the monopole and quadrupole perturbation orders. Explicitly, using the definition of  $v^\mu$  from Eq. (7), we can also compute the expressions for  $\mathcal{T}_x$  as follows

$$\begin{aligned} \mathcal{T}_x = \mathcal{P}_x - & \frac{C \left[ (\gamma-1) \left(\frac{p_r}{\kappa}\right)^{1/\gamma} + \gamma p_r \right] p'_r}{\gamma(\gamma-1) \sqrt{\frac{r}{r-2m}} p_r} \mathcal{P}_x \\ & + \frac{C \left[ (\gamma-1) \left(\frac{p_r}{\kappa}\right)^{1/\gamma} + p_r \right] [m_x p'_r - (r-2m) \mathcal{P}'_x]}{(\gamma-1) \sqrt{r(r-2m)}}. \end{aligned} \quad (65)$$

Alternatively, one can introduce a rotating generalization to the rest mass density, in the following form

$$\mathcal{Z} = \rho_0 + \Omega^2 \mathcal{Z}_0 + \Omega^2 P_2(\cos(\theta)) \mathcal{Z}_2, \quad (66)$$

and then write

$$\mathcal{P}_x = \kappa \gamma \rho_0^{\gamma-1} \mathcal{Z}_x, \quad (67)$$

$$\mathcal{E}_x = \left( 1 + \frac{\kappa \gamma \rho_0^{\gamma-1}}{\gamma-1} \right) \mathcal{Z}_x, \quad (68)$$

$$\begin{aligned} \mathcal{T}_x = & \gamma \kappa \rho_0^{\gamma-1} \mathcal{Z}_x \\ & - \frac{C \gamma \kappa \rho_0^{\gamma-1} \rho_0' \left[ \gamma(\gamma-1) + (2\gamma-1) \kappa \rho_0^{\gamma-1} \right]}{(\gamma-1) \sqrt{\frac{r}{r-2m}}} \mathcal{Z}_x \\ & + \frac{C \gamma \kappa \rho_0^\gamma \left( \gamma-1 + \kappa \rho_0^{\gamma-1} \right) [\rho_0' m_x - (r-2m) \mathcal{Z}'_x]}{(\gamma-1) \sqrt{r(r-2m)}}. \end{aligned} \quad (69)$$

### IV. NUMERICAL RESULTS

The extended Hartle structure equations, summarized in Sec. II, were numerically integrated using methods similar to those employed in [1] to study anisotropic homogeneous Bowers-Liang spheres in slow rotation. In contrast to the homogeneous model, the EoSs considered here do not permit an analytic solution describing the nonrotating configuration. Thus, for a given triplet  $(n, \kappa, C)$ , we determined the bounding radius  $R$  and total mass  $M(R)$  by numerically integrating the hydrostatic equilibrium equation (11), specifically using formulations (60) and (61), varying the central rest-mass density  $\rho_0(0) = \rho_{0c}$  as the only free parameter of the solution. The stellar surface  $R$  was found by the condition  $p_r(R) = 0$ . Once the total mass and radius were obtained, we computed the configuration's compactness,  $GM/(c^2 R)$ .

The central value of the metric function  $e^\nu$  was determined by numerically integrating Eq. (14) using, either the shooting method [or defining an auxiliary function analogously to the  $(h_0, H_0)$  construction in our consistency check codes] and setting the matching condition at the boundary with the exterior Schwarzschild metric. Once the nonrotating configuration was fully determined, i.e.,  $R$ ,  $M(R)$ ,  $\nu(r)$  and  $\lambda(r)$  are known for the background solution, we solved for the monopole and quadrupole perturbation functions by simultaneously integrating the extended structure equations with their respective initial conditions. For instance, for the monopole sector we integrated simultaneously the coupled ODEs system, Eqs. (19), (23), (24), and (25). Similarly, for the quadrupole sector, we integrated the system (31)-(35) in the representation  $(h_2, k_2, \mathcal{Z}_2, \Upsilon)$ . The principal results of the numerical integrations are illustrated in Figs. 1-19. We introduce dimensionless variables, with units specified in the corresponding figure descriptions. Although the central rest-mass density  $\rho_{0c}$  is the only free parameter of the solution, we plotted the various perturbation functions against the compactness, to facilitate the comparison with some of the results reported by [33] for slowly rotating isotropic polytropes.

As a consistency check, we also constructed additional codes to solve the background sector and import the background quantities as Mathematica's [37] 'interpolating functions' for solving the perturbations. For the monopole sector, we implemented these codes for the EoSs (64) and (65) in terms of  $\mathcal{P}_0$ , and  $\mathcal{Z}_0$ . For the quadrupole sector, we constructed multiple backup codes, one solving four ODEs in terms of the functions  $(h_2, k_2, \mathcal{Z}_2, \Upsilon)$ , another solving four ODEs in terms of the functions  $(h_2, k_2, \mathcal{P}_2, \Upsilon)$ , and a third reducing the system to second-order equations involving only  $h_2$  and  $k_2$ .

### A. Mass-Radius diagram of $\mathcal{C}$ -stars

A sequence of equilibrium  $\mathcal{C}$ -star configurations, with fixed values of the parameters  $n$ ,  $\kappa$  and  $\mathcal{C}$ , can be constructed by integrating the ATOV system (60) and (61), varying the central rest-mass density  $\rho_{0c}$  as a free parameter. Following this procedure, we obtained the mass-radius diagram for  $\mathcal{C}$ -stars, shown in Fig. 1, for various values of the anisotropy parameter  $\mathcal{C}$ . Henceforth we focus on a configuration with  $\kappa = 100$ , and  $n = 1$ , which reproduces the reference configuration, in the isotropic case, presented in [38]. The maximum of each curve marks the onset of instability, as determined by the standard  $M(R)$  method [26, 39]. In all subsequent computations, we restrict ourselves to configurations with  $\rho_{0c}$  below the critical value for stability.

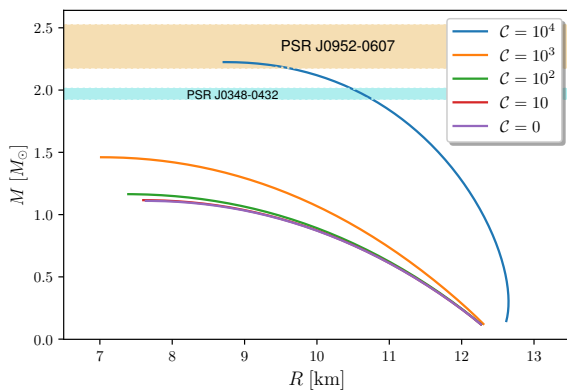


FIG. 1. Mass-radius diagram for  $\mathcal{C}$ -stars, for different values of the anisotropy parameter  $\mathcal{C}$ . We consider a polytrope with  $\kappa = 100$  and  $n = 1$ . The maximum of the curves indicates the onset of instability. The color filled horizontal bands indicate the observational mass constraints from the pulsars PSR J0952-0607 [40] and PSR J0348-0432 [41].

In Fig. 2, we show the compactness  $GM/(c^2R)$ , as a function of  $\rho_{0c}$ , for different values of the anisotropy parameter  $\mathcal{C}$ . The integration was halted at the critical value of  $\rho_{0c}$  for the onset of instability. Notably, the maximum compactness we found for radial stability in the isotropic case ( $\mathcal{C} = 0$ ), closely matches the value reported by [33], which was obtained through a static stability analysis of isentropic gas spheres. Note that for a given value of the central rest-mass density, an increase in the anisotropy increases the compactness.

### B. Frame dragging and moment of inertia

To determine the dragging of the inertial frames in  $\mathcal{C}$ -stars, we numerically integrated Eq. (19) with the boundary conditions (21), starting from the origin (or rather from some cut-off value  $r_0 = 10^{-6}$ ), up the surface  $R$ . This was done for various configurations and different

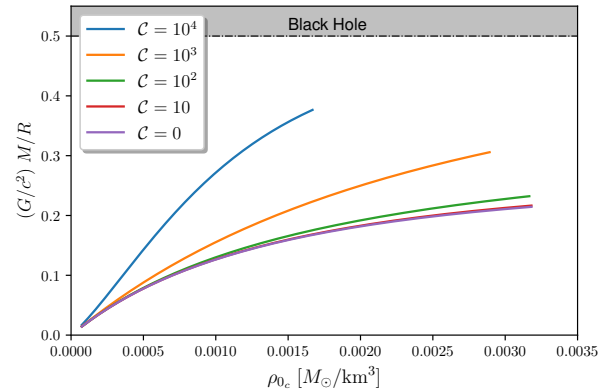


FIG. 2. Compactness  $GM/c^2R$ , as a function of the central density, for the same values of the anisotropic parameter  $\mathcal{C}$  as in the left panel. Note that, for a given value of the central density, as the anisotropy increases, the compactness also increases.

values of the anisotropy parameter  $\mathcal{C}$ .

Following the conventions from [1], we measure  $\varpi$  in units of  $J/R_S^3$ , where  $R_S \equiv 2GM/c^2$  is the Schwarzschild radius. Thus it is convenient to introduce the quantity  $\tilde{\varpi} \equiv \varpi/(J/R_S^3)$ . In Fig. 3 we display the variation of the function  $\varpi$  through the body, in units of  $\Omega$ , for different configurations. Following [29] we consider the anisotropy parameter values:  $\mathcal{C} = \{0, 10^2, 10^3, 10^4\}$ . We observe that as the compactness increases,  $\varpi$  at the origin approaches zero. We point out that the configurations we are considering here are always below the critical compactness for stability, as given by the  $M(R)$  method.

In the left panel of Fig. 4, we show the surface value  $\tilde{\varpi}(R)$ , as a function of compactness, for various values of the anisotropy parameter  $\mathcal{C}$ . For low compactness, we observe that  $\tilde{\varpi}(R) \rightarrow 0$ , implying  $\omega \approx \Omega$ , as expected in the Newtonian limit. The right panel of the same figure shows the central value  $\varpi(0)$ , in units of  $\Omega$ , as a function of compactness for the anisotropy values as in the left panel. For a given anisotropy, as the compactness increases,  $\varpi(0)$  decreases. Notably, in highly anisotropic configurations,  $\varpi(0)$  appears to approach zero, suggesting that in such cases  $\omega(0)$  approaches the angular velocity of the fluid  $\Omega$ . This same behavior was also observed in Schwarzschild stars at the Buchdahl limit [42] and in Bowers-Liang spheres [1]. However, since our analysis is constrained by stability criteria, we do not explore configurations near the point where pressure diverges, ensuring that  $\varpi(0)$  remains strictly above zero in all cases considered.

In Fig. 5 we present the normalized moment of inertia  $I/MR^2$ , as a function of the compactness for varying values of  $\mathcal{C}$ . In the isotropic case ( $\mathcal{C} = 0$ ), our results show excellent agreement with those reported by [33] for slowly rotating polytropes with  $\gamma = 2$ . In the low compactness limit, we observe that all the curves converge to the New-

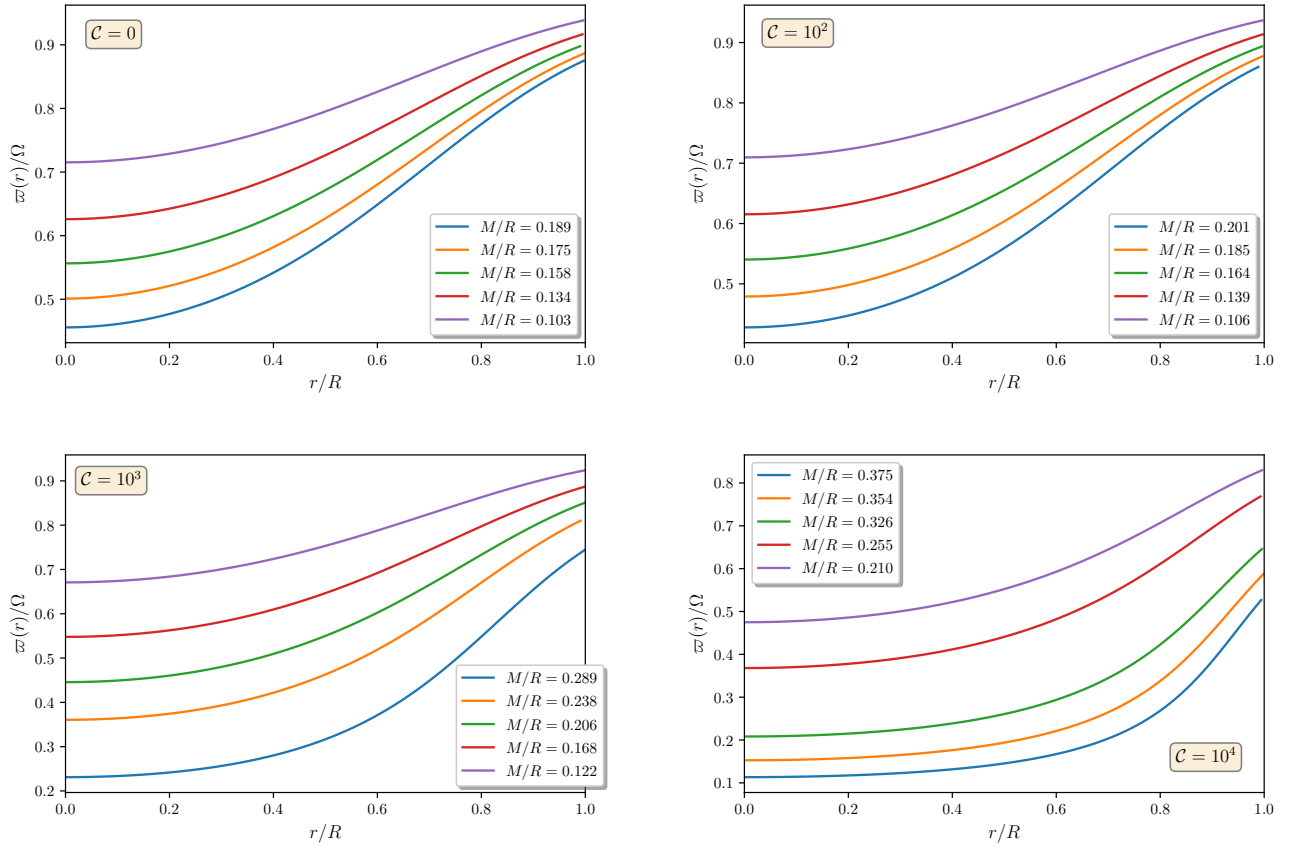


FIG. 3. Radial profiles of the  $\varpi$  function, in the unit  $\Omega$ , for different compactness, for various values of the anisotropy parameter  $\mathcal{C}$ . Observe that as the compactness increases,  $\varpi$  at the origin decreases. Notice that the highest compactness configurations we consider here are determined by the  $M(R)$  stability criteria, so we do not have configurations especially close to the limiting compactness when the central pressure diverges for that particular EoS, nor to the BH limit.

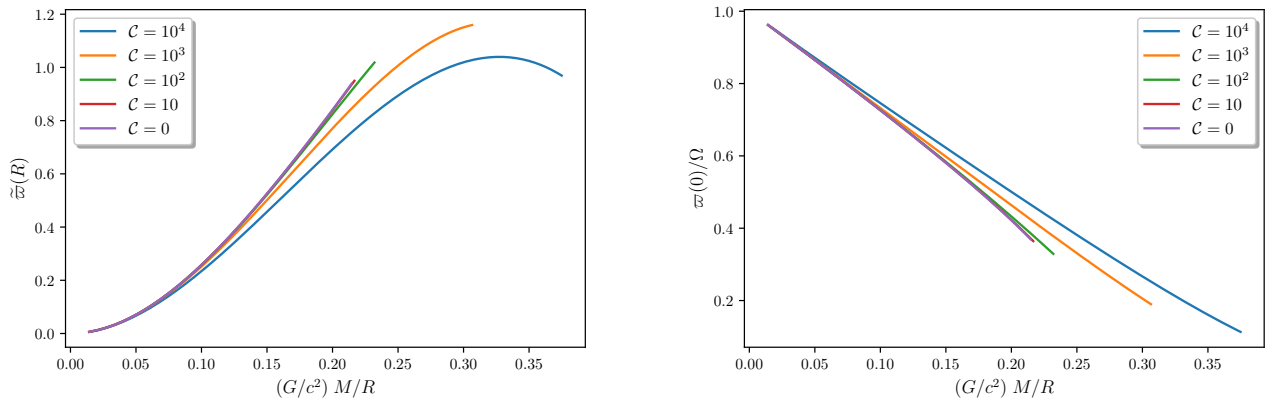


FIG. 4. **Left panel:** Surface value of the  $\tilde{\varpi}$  function, as a function of compactness, for various values of the anisotropy parameter  $\mathcal{C}$ . **Right panel:** Function  $\varpi$  evaluated at the origin, as a function of the compactness, for the same values of  $\mathcal{C}$  as in the left panel. We measure  $\varpi(0)$  in the unit  $\Omega$ . Observe that at any given anisotropy,  $\varpi(0)$  decreases with compactness, and at any given compactness  $\varpi(0)$  increases with anisotropy.

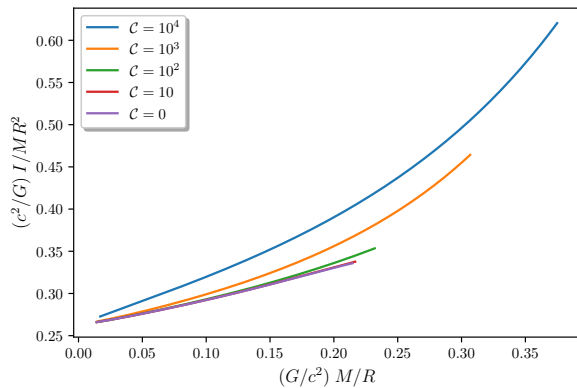


FIG. 5. Normalized moment of inertia  $I/MR^2$  of  $\mathcal{C}$ -stars, as a function of the compactness, for various values of the anisotropy parameter  $\mathcal{C}$ .

tonian value  $I/MR^2 = 2(\pi^2 - 6)/3\pi^2 = 0.261^3$ . For fixed compactness, an increase in the anisotropy parameter  $\mathcal{C}$  leads to an increase in the normalized moment of inertia. While one may expect that as anisotropy increases, the maximum allowed compactness approaches the BH limit,—implying  $I/MR^2 \rightarrow 1$ —the solutions considered here are constrained by the stability criterion. Consequently, the strict BH limit cannot be explored within the scope of these configurations. The moment of inertia of  $\mathcal{C}$ -stars was also reported by [34].

### C. Monopole sector

The monopole sector is governed by Eqs. (23), (24), and (25), involving the metric perturbation functions  $m_0$ , and  $h_0$ , and the EMT eigenvalue perturbation functions  $\mathcal{E}_0$ ,  $\mathcal{P}_0$ , and  $\mathcal{T}_0$ . The exterior spacetime depends on the parameter  $\delta M$  (see Eq. (27)), which is determined by the monopole sector. The system's monopole deformation is given by  $\xi_0$ .

#### 1. Behavior of the monopole perturbation functions

We can draw some observations from the EoSs governing the  $\mathcal{C}$ -stars, and the EoSs for the perturbations, namely, Eqs. (67), (68), and (69). The perturbation functions  $\mathcal{P}_x$  and  $\mathcal{T}_x$  typically go to zero at the surface, as both  $p_r$  and  $\rho_0$  vanish there. On the other hand,  $\mathcal{E}_x$  and  $\mathcal{Z}_x$  tend to the same finite value at the boundary. This also leads to drawing some conclusions about the deformation  $\xi_0$ . If the rest mass density at the surface goes to zero,

at least linearly, i.e.

$$\rho_0(r \approx R^-) = \rho_0^a(R - r) + \dots, \quad (70)$$

then

$$p_r(r \approx R^-) = \kappa \rho_0^a(R - r)^2 + \dots, \quad (71)$$

thus  $p'_r(r \approx R^-) = -2\kappa \rho_0^a(R - r)$ . This implies that  $\xi_0 = -\mathcal{P}_0/p'_r(r \rightarrow R^-)$  would formally be an ill-defined, and problematic for numeric computation,  $0/0$  form. However, using Eq. (70) for the behavior near the surface, as well as the postulated expansions  $m(r \approx R^-) = M + m_a(R - r) + \dots$ , and,  $\nu_0(r \approx R^-) = \nu_R + \nu_a(r - R) + \dots$ , the background Einstein equations (11)-(14) and the EoSs (54), and (57), with  $\kappa = 100$ , and  $n = 1$ , imply that a solution exists with

$$\rho_0^a = \frac{M}{200R(R - 2M)}, \quad (72)$$

therefore  $p_r \approx \frac{M^2}{400R^2(R - 2M)^2}(r - R)^2$  and

$$p'_r(r \approx R^-) = \frac{M^2}{200R^2(R - 2M)^2}(r - R) + \dots. \quad (73)$$

Using Eq. (67), together with Eqs. (70), (72), and (73), we can explicitly divide the lowest order terms in the series expansions to obtain

$$\begin{aligned} \xi_x &= -\frac{\mathcal{P}_x(R)}{p'_r(r \rightarrow R^-)} \\ &= -\frac{k\gamma\rho_0^{\gamma-1}\mathcal{Z}_x}{p'_r(r \rightarrow R^-)} = \frac{200R(R - 2M)}{M}\mathcal{Z}_x(R), \end{aligned} \quad (74)$$

which is readily computable.

#### 2. Results for the monopole perturbations

Let us now discuss our results for the monopole perturbations of  $\mathcal{C}$ -stars. To study the spherical deformations, we numerically integrated Eqs. (23)-(25), with the initial conditions  $h_0(0) = m_0(0) = \mathcal{P}_0(0) = 0$ . Following the conventions of [1], it is convenient to define the following quantities

$$\begin{aligned} \widetilde{h}_0 &\equiv \frac{h_0}{(J^2/R_S^4)}, & \widetilde{m}_0 &\equiv \frac{m_0}{(J^2/R_S^3)}, & \widetilde{\mathcal{P}}_0 &\equiv \frac{\mathcal{P}_0}{(J^2/R_S^6)}, \\ \widetilde{\mathcal{E}}_0 &\equiv \frac{\mathcal{E}_0}{(J^2/R_S^6)}, & \widetilde{\mathcal{Z}}_0 &\equiv \frac{\mathcal{Z}_0}{(J^2/R_S^6)}. \end{aligned} \quad (75)$$

In Fig. 6 we display the surface value of the perturbation function  $\widetilde{m}_0$ , as a function of compactness, for various values of  $\mathcal{C}$ . Observe that the various curves show a local maximum, then  $\widetilde{m}_0$  decreases as the compactness increases. Figure 7 shows the perturbation functions  $\widetilde{\mathcal{E}}_0(R)$  and  $\widetilde{\mathcal{Z}}_0(R)$ , evaluated at the surface, for varying compactness. Note that, according to Eq. (68), both functions approach the same value at the surface, since the rest mass

<sup>3</sup> This result comes from solving the Newtonian hydrostatic equilibrium equation, for an isotropic polytrope with  $n = 1$ .

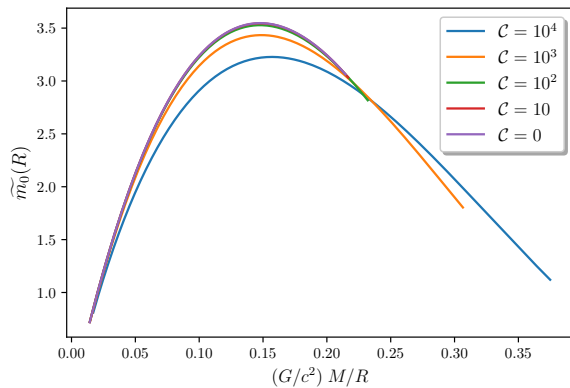


FIG. 6. Perturbation function  $\tilde{m}_0(R)$ , evaluated at the surface, as a function of compactness, for various values of the anisotropy parameter  $\mathcal{C}$ .

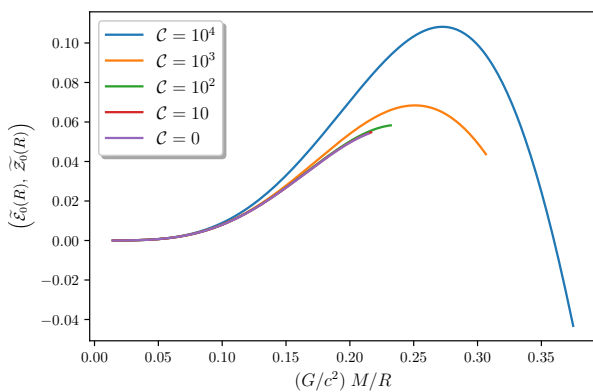


FIG. 7. Surface value of the perturbation functions  $\tilde{\mathcal{E}}_0(R)$ , and  $\tilde{\mathcal{Z}}_0(R)$ , against compactness, for various values of the anisotropy parameter  $\mathcal{C}$ .

density vanishes there. We consider the same values of the anisotropy parameter as in Fig. 6. For the curves  $\mathcal{C} = \{0, 10, 10^2\}$  observe that the perturbation functions increase with compactness. A slightly different behavior is observed in the cases  $\mathcal{C} = \{10^3, 10^4\}$ , where the curves show a local maximum, and then decrease before reaching the critical point for instability. One may suspect that the maximum of the curves with low  $\mathcal{C}$  will be found beyond the point of instability, however, we remark that this regime cannot be explored within these solutions.

It is worthwhile to mention that for  $n = 1$  and  $\kappa = 100$ , the perturbations  $\mathcal{P}_x$  and  $\mathcal{T}_x$  typically vanish at the surface, as they are proportional to  $p_r$  and  $\rho_0$  which also go to zero at the surface. In contrast,  $\mathcal{E}$  and  $\mathcal{Z}$  approach the same finite value. The  $l = 0$  deformation of the boundary  $\xi_0/R$  is shown in Fig. 8, as a function of compactness, for varying anisotropy parameter  $\mathcal{C}$ . The function  $\xi_0/R$  is measured in units of  $J^2/R_S^4$ . Observe that the various curves show a local maximum. It is noteworthy

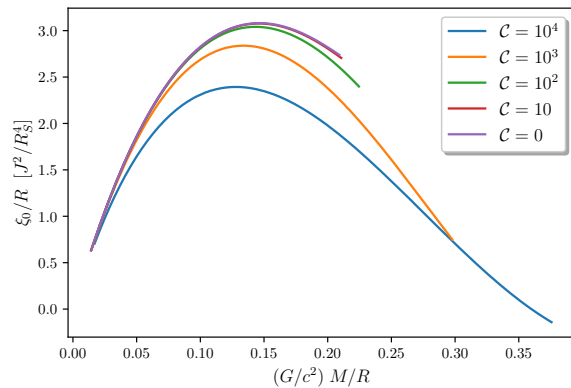


FIG. 8. Surface values of the spherical deformation function  $\xi_0/R$ , as a function of compactness, for various values of the anisotropy parameter  $\mathcal{C}$ . We measure  $\xi_0/R$  in units of  $J^2/R_S^4$ .

thy that for the highly anisotropic case  $\mathcal{C} = 10^4$ ,  $\xi_0/R$  transitions to negative values beyond  $M/R \sim 0.35$ . This is remarkably similar to highly anisotropic Bowers-Liang spheres [1] where we found the same behavior and a subsequent approach to zero.

As it was discussed in [1], the computation of the true perturbation function  $h_0$  requires a few steps. First, one finds  $H_0$  as a solution to Eqs. (24) and (26), assuming a certain integration constant. Then, one determines the corresponding integration constant, such that the interior solution matches the exterior solution given by

$$h_0 = \frac{1}{r - 2M} \left( \frac{J^2}{r^3} - \delta M \right), \quad r > R. \quad (76)$$

Since the background  $g_{tt}$  is finite and nonzero, there will be no mismatch with the  $h_0$  functions. Figure 9 displays the perturbation functions  $H_0$  and  $h_0$ , evaluated at the surface, for various anisotropy values  $\mathcal{C}$ . Observe that, for a fixed compactness, as the anisotropy increases  $H_0(R)$  decreases.

In Fig. 10 we display the profiles of the constant  $h_c$ , defined by Eq. (26), as a function of compactness for varying values of  $\mathcal{C}$ . The constant  $h_c$  is measured in units of  $J^2/R_S^4$ . We observe that, for a fixed compactness,  $h_c$  increases with anisotropy. Conversely, for a given anisotropy,  $h_c$  decreases as compactness increases. For the most compact configurations tested, highly anisotropic systems approach the critical value for instability, with  $h_c \rightarrow -6J^2/R_S^4$  approximately. It is noteworthy that this behavior was also observed in sub-Buchdahl Schwarzschild stars in the gravastar limit [42], as well as Bowers-Liang spheres [1].

Finally, from Eq. (29) we determine the change in mass  $\delta M$  which we present in Fig. 11, as a function of compactness, for various values of the parameter  $\mathcal{C}$ . The quantity  $\delta M/M$  is measured in units of  $J^2/R_S^4$ .

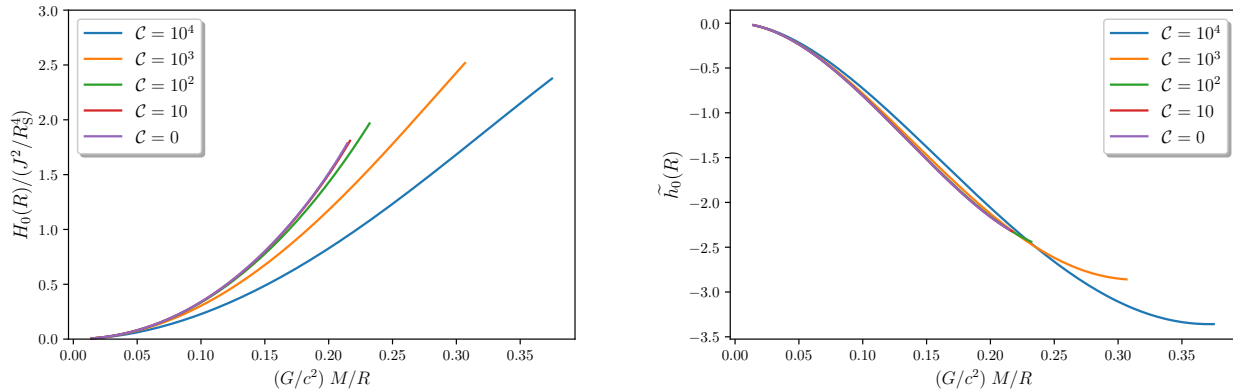


FIG. 9. **Left panel:** surface value of the auxiliary function  $H_0$  (in units of  $J^2/R_S^4$ ), as a function of compactness, for various values of anisotropy. For a given value of compactness, as  $\mathcal{C}$  increases,  $H_0(R)$  decreases. **Right panel:** surface value of the perturbation function  $\tilde{h}_0(R)$ , as a function of compactness, for the same values of the anisotropy parameter  $\mathcal{C}$  as in the left panel.

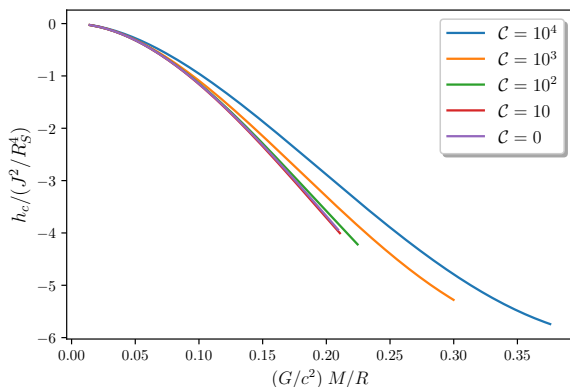


FIG. 10. Profiles of the constant  $h_c$ , as a function of compactness, for various values of the anisotropy parameter  $\mathcal{C}$ . We measure  $h_c$  in units of  $J^2/R_S^4$ . For highly anisotropic configurations, as the compactness approaches its critical value for stability,  $h_c \rightarrow -6J^2/R_S^4$ , approximately.

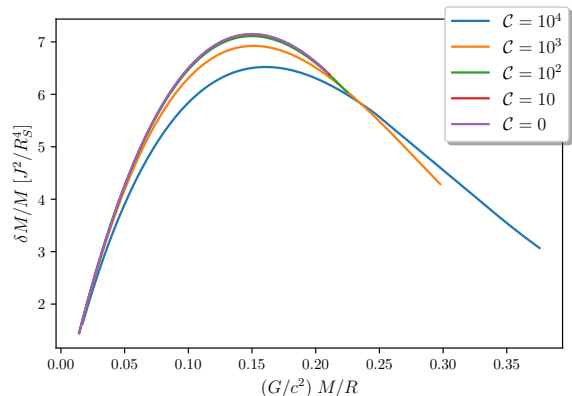


FIG. 11. Change of mass  $\delta M/M$  (in units of  $J^2/R_S^4$ ), as a function of compactness, for various values of the anisotropy parameter  $\mathcal{C}$ .

#### D. Quadrupole sector

The quadrupole perturbations are determined by Eqs. (31), (32), (34) and (35), which features the metric perturbation functions  $h_2$ ,  $k_2$ , and  $m_2$ , the EMT eigenvalue perturbations  $\mathcal{E}_2$ ,  $\mathcal{P}_2$ , and  $\mathcal{T}_2$ , and the eigenvector perturbation function  $\Upsilon$ . The surface deformation can be parameterized by  $\xi_2$  or  $\epsilon$ .

Similarly to the monopole perturbations, the EoSs give that  $\mathcal{P}_2$  and  $\mathcal{T}_2$  vanish at the surface, and  $\mathcal{E}_2$  and  $\mathcal{Z}_2$  approach some constant value. The surface deformations  $\epsilon$  and  $\xi_2$  involve problematic  $0/0$  terms, however, equation (74) allows for  $\xi_2$ , and hence  $\epsilon$  to be computed without any issues.

##### 1. Behavior of the quadrupole perturbation functions

In [1], we found that the Einstein equations impose specific constraints on the behavior of perturbations in general well-behaved systems. In particular, the lowest-order terms in  $h_2$ ,  $k_2$ ,  $\mathcal{P}_2$ , and  $\mathcal{T}_2$  behave as  $O(r^2)$ , while  $\Upsilon$  behaves as  $O(r)$ . Moreover, the leading coefficients of the perturbations  $\mathcal{P}_2$ ,  $\mathcal{T}_2$ , and  $\Upsilon$  are related to the quadratic and quartic components of  $h_2$  and  $k_2$ . A similar analysis can be performed for the  $\mathcal{C}$ -star, however, the isotropic and anisotropic cases must be treated separately due to their different behavior near the origin in the background solution.

*a. The isotropic case* For the isotropic case, we find that

$$h_2^b + k_2^b = \frac{2\pi}{3} \left\{ e^{-2\nu_c} \varpi_c^2 \left[ \left( \frac{p_c}{\kappa} \right)^{1/\gamma} + \frac{\gamma p_c}{\gamma - 1} \right] + k_2^a \left[ \left( \frac{p_c}{\kappa} \right)^{1/\gamma} + \frac{(3\gamma - 2)p_c}{\gamma - 1} \right] \right\}, \quad (77)$$

where  $\rho_c = (p_c/\kappa)^{1/\gamma} + p_c/(\gamma - 1)$ . The surviving lowest-order terms, for well-behaved systems, become

$$\mathcal{P}_2^{(P)} = \mathcal{T}_2^{(P)} = \left( k_2^a - \frac{1}{3} e^{-2\nu_c} \varpi_c^2 \right) \times \left[ \left( \frac{p_c}{\kappa} \right)^{1/\gamma} + \frac{\gamma p_c}{\gamma - 1} \right] r^2 + \dots, \quad (78)$$

$$k_2^{(P)} = k_2^a r^2 + \dots, \quad (79)$$

$$h_2^{(P)} = -k_2^a r^2 + \dots, \quad (80)$$

$$\Upsilon^{(P)} = 0. \quad (81)$$

Notice that  $\mathcal{P}_2 = \mathcal{T}_2$  and  $\Upsilon = 0$ , as expected for isotropy.

*b. The anisotropic case* In the anisotropic case, using series solutions for the background and quadrupole perturbation functions we obtain

$$h_2^b + k_2^b = \frac{4\pi}{3} \left\{ e^{-2\nu_c} \varpi_c^2 \left[ \left( \frac{p_c}{\kappa} \right)^{1/\gamma} + \frac{\gamma p_c}{\gamma - 1} \right] - k_2^a \left[ \left( \frac{p_c}{\kappa} \right)^{1/\gamma} + \frac{p_c}{\gamma - 1} \right] \right\}, \quad (82)$$

such that the surviving lowest-order terms, for general well-behaved systems, become

$$\mathcal{P}_2^{(P)} = 0, \quad (83)$$

$$\mathcal{T}_2^{(P)} = -4 \left( k_2^a - \frac{\varpi_c^2}{3e^{2\nu_c}} \right) \left[ \left( \frac{p_c}{\kappa} \right)^{1/\gamma} + \frac{\gamma p_c}{\gamma - 1} \right] r^2 + \dots, \quad (84)$$

$$k_2^{(P)} = k_2^a r^2 + \dots, \quad (85)$$

$$h_2^{(P)} = -k_2^a r^2 + \dots, \quad (86)$$

$$\Upsilon^{(P)} = - \left( 3k_2^a - \frac{\varpi_c^2}{e^{2\nu_c}} \right) \left[ \left( \frac{p_c}{\kappa} \right)^{1/\gamma} + \frac{\gamma p_c}{\gamma - 1} \right] r + \dots. \quad (87)$$

Note that for the anisotropic  $\mathcal{C}$ -star,  $\mathcal{P}_2$ , similar to  $p_r$  (see Appendix A), does not possess quadratic terms in its series expansions near the origin. Interestingly, the anisotropic  $\mathcal{C}$ -star has cubic terms in the  $h_2$  and  $k_2$  obeying

$$k_2(r^3) = -h_2(r^3) = \frac{4(\gamma - 1) (3k_2^a - e^{-2\nu_0} \varpi_c^2)}{9\mathcal{C} [p_c + (\gamma - 1) (p_c/\kappa)^{1/\gamma}]}. \quad (88)$$

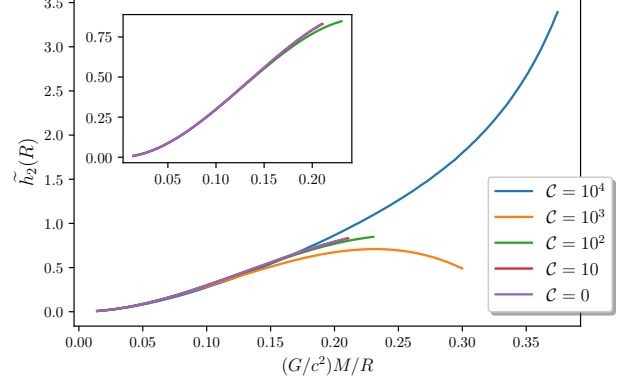


FIG. 12. Surface value  $\widetilde{h}_2(R)$ , as a function of compactness, for various values of the anisotropy  $\mathcal{C}$ .

## 2. Results for the quadrupole perturbations

We numerically integrated the quadrupole perturbation functions, Eqs. (31), (32), (34), and (35), from the origin (or rather some cutoff value  $r_0 = 10^{-6}$ ) up to the surface  $R$ . For high anisotropies, we had to increase the cutoff value to  $10^{-5}$  to avoid numerical instabilities.

Following the conventions employed in [1] we define the following quantities

$$\widetilde{h}_2 \equiv \frac{h_2}{(J^2/R_S^4)}, \quad \widetilde{k}_2 \equiv \frac{k_2}{(J^2/R_S^4)}, \quad (89a)$$

$$\widetilde{m}_2 \equiv \frac{m_2}{(J^2/R_S^3)}, \quad \widetilde{\mathcal{P}}_2 \equiv \frac{\mathcal{P}_2}{(J^2/R_S^6)}, \quad (89b)$$

$$\widetilde{\mathcal{T}}_2 \equiv \frac{\mathcal{T}_2}{(J^2/R_S^6)}, \quad \widetilde{\mathcal{Z}}_2 \equiv \frac{\mathcal{Z}_2}{(J^2/R_S^6)}. \quad (89c)$$

In Fig. 12 we plot the surface value  $\widetilde{h}_2(R)$ , as a function of compactness, for different values of the anisotropy parameter  $\mathcal{C}$ . Observe how the curve  $\mathcal{C} = 10^4$  grows rapidly as the compactness approaches the critical value for instability.

In Fig. 13 we show the surface value  $\widetilde{k}_2(R)$ , as a function of compactness, for different values of the anisotropy parameter  $\mathcal{C}$ . Observe that the function  $\widetilde{k}_2(R)$  takes negative values. Moreover, the curve  $\mathcal{C} = 10^4$  decreases rapidly as the compactness approaches the critical value for instability.

Figure 14 displays the value of  $\widetilde{m}_2$  at the surface, as a function of compactness, for various values of anisotropy. Observe that the various curves show a local minimum. The curve  $10^3$  crosses toward positive values when  $M/R \sim 0.28$ .

Figure 15 shows the surface values of the perturbation functions  $\widetilde{\mathcal{E}}_2(R)$  and  $\widetilde{\mathcal{Z}}_2(R)$  as a function of compactness for various values of the anisotropy parameter  $\mathcal{C}$ . The inset highlights the curves corresponding to

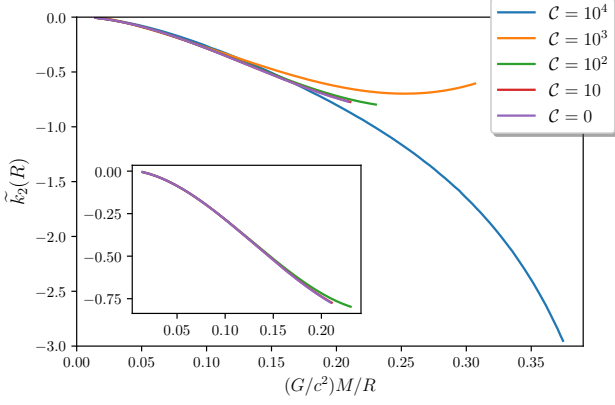


FIG. 13. Surface value  $\tilde{k}_2(R)$ , as a function of compactness, for various values of the anisotropy  $\mathcal{C}$ .

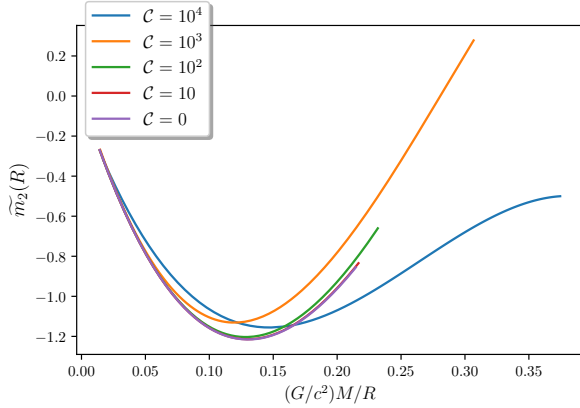


FIG. 14. Surface value  $\tilde{m}_2(R)$ , as a function of compactness, for various values of the anisotropy  $\mathcal{C}$ .

$\mathcal{C} = \{0, 10, 10^2\}$  to enhance visualization. According to Eq. (68), the surface values of  $\tilde{\mathcal{E}}_2$  and  $\tilde{\mathcal{Z}}_2$  coincide since the rest mass density vanishes at the boundary.

Figure 16 displays the quadrupole deformation function  $-\xi_2(R)/R$  (in units of  $J^2/R_S^4$ ), as a function of compactness for various values of the anisotropy parameter  $\mathcal{C}$ . The inset highlights the curves for  $\mathcal{C} = \{0, 10, 10^2\}$  for better visualization. Notably, while the configurations with  $\mathcal{C} = \{0, 10, 10^2\}$  maintain positive values, the case with  $\mathcal{C} = 10^3$  transitions to negative values for  $M/R \sim 0.18$ . Similarly, for the highly anisotropic case  $\mathcal{C} = 10^4$ , the function turns negative when  $M/R$  surpasses approximately 0.09. Interestingly, this sign change in the quadrupole deformation function was also observed in highly anisotropic Bowers-Liang spheres [1].

The ellipticity of the boundary, shown in Fig. 17, follows a similar trend to the  $-\xi_2$  curves. With the exception of the isotropic case, all curves exhibit a maximum, and higher anisotropy curves lie below those with lower anisotropy. Notably, for highly anisotropic cases, the ellipticity takes negative values, indicating that these

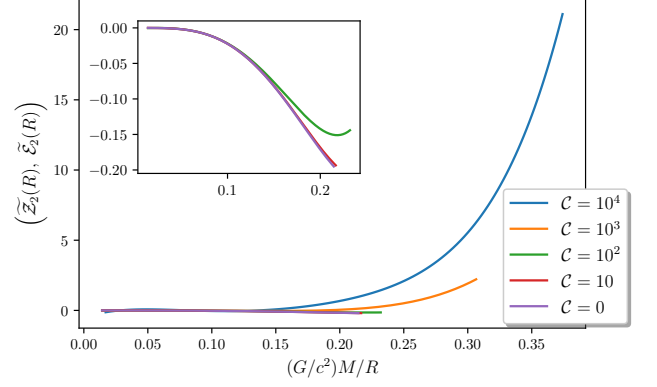


FIG. 15. Surface value of the perturbation functions  $\tilde{\mathcal{E}}_2(R)$  and  $\tilde{\mathcal{Z}}_2(R)$ , as a function of compactness, for various values of the anisotropy  $\mathcal{C}$ . The inset enhances the curves  $\mathcal{C} = \{0, 10, 10^2\}$ .

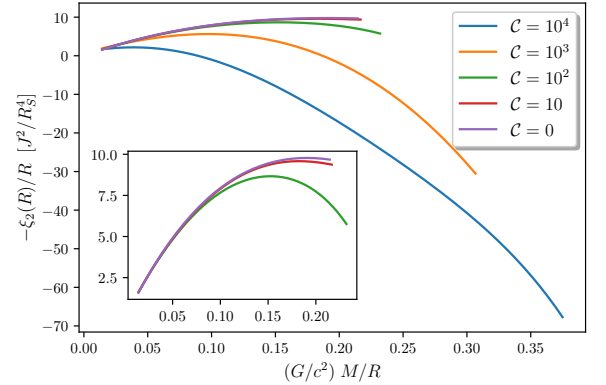


FIG. 16. The quadrupole perturbation function  $-\xi_2(R)/R$ , is shown as a function of compactness, for various values of the anisotropy parameter  $\mathcal{C}$ . The inset provides a detailed view of the curves for  $\mathcal{C} = \{0, 10, 10^2\}$ . Observe that the highly anisotropic cases  $\mathcal{C} = \{10^3, 10^4\}$ , transition to negative values.

configurations become prolate rather than oblate. Although [32], in their study of slowly rotating piecewise polytropes with a quasi-local anisotropic EoS, did not analyze the ellipticity of these configurations, they found that the mass quadrupole moment changes sign for high anisotropies and compactness. Based on this, they concluded that such configurations are prolate. Thus, these findings, along with our results, suggest that highly anisotropic systems frequently tend to be prolate rather than oblate.

It is worthwhile to mention that we obtained a slight difference, between the various codes, in the surface values of  $\epsilon$  and the  $\xi_2$  function for  $\mathcal{C} = \{10^3, 10^4\}$  at high compactnesses due to the rapidly growing behaviour of the function  $\mathcal{Z}_2$  in the vicinity of the star surface.

The surface values of the eigenvector perturbation

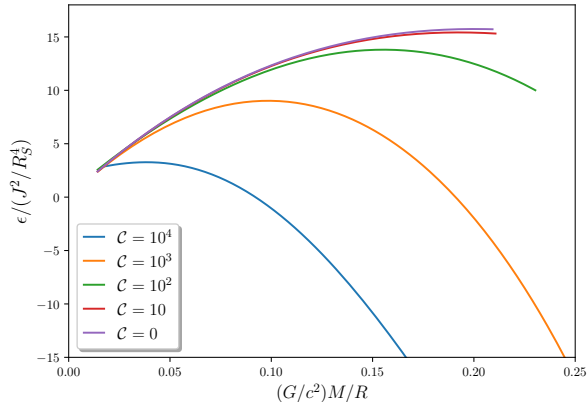


FIG. 17. Ellipticity of the bounding surface, against compactness, for various values of the anisotropy parameter  $\mathcal{C}$ . We measure the ellipticity in units of  $J^2/R_S^4$ . Observe that the curves  $\mathcal{C} = \{10^3, 10^4\}$  transition to negative values of ellipticity (prolate), beyond certain compactness.

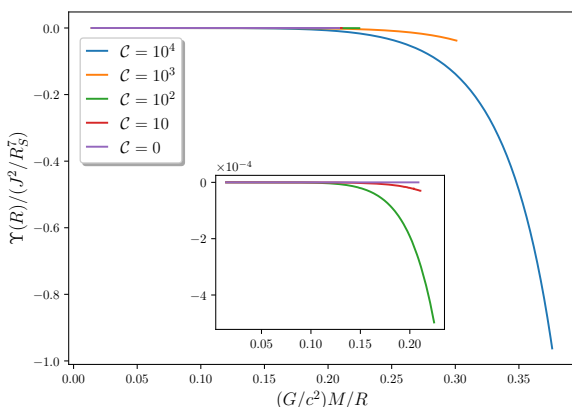


FIG. 18. Profiles of the auxiliary function  $\Upsilon$ , evaluated at the surface, as a function of compactness. We plot different values of the anisotropy parameter  $\mathcal{C}$ . The inset provides an enhanced view of the curves  $\mathcal{C} = \{0, 10, 10^2\}$ . Observe that in the isotropic case  $\mathcal{C} = 0$ ,  $\Upsilon$  is identically zero.

function  $\Upsilon$  are shown in Fig. 18. Notice that  $\Upsilon$  is identically 0 for the isotropic case and remains relatively small for most of the cases considered. Moreover, it appears to monotonically become increasingly negative with both compactness and  $\mathcal{C}$ .

While the ellipticity and  $\xi_2$  function change sign, for certain configurations, the reduced quadrupole moment, or ‘Kerr factor’  $QM/J^2$ , depicted in Fig. 19, remains positive across all tested cases. This indicates that even when the outer boundary exhibits a prolate deformation, in some instances, the overall gravitational effect of the mass distribution still corresponds to an oblate configuration. An intriguing result is that, for  $\mathcal{C} = 10^3$ , the

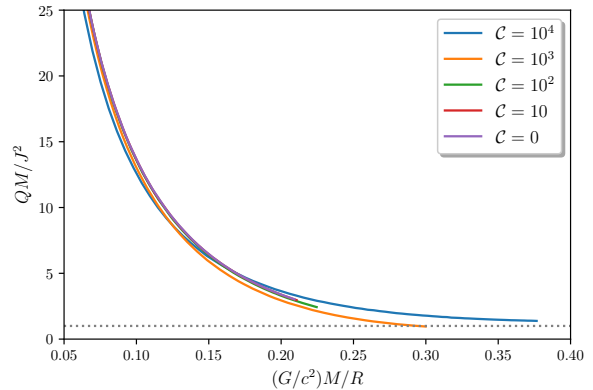


FIG. 19. Reduced quadrupole moment, or ‘Kerr factor’  $QM/J^2$ , as a function of compactness, for various values of the parameter  $\mathcal{C}$ . The grey dotted line indicates the Kerr BH value  $QM/J^2 = 1$ .

Kerr factor drops slightly below the Kerr BH value (i.e.  $QM/J^2 < 1$ ) at the critical stability threshold, whereas the  $\mathcal{C} = 10^4$  curve stays above one (gray dotted line), and appears to approach the Kerr BH value. Additionally, all  $Q$  curves decrease monotonically as compactness increases.

## V. DISCUSSION

In this work, we investigated the structure and integral properties of slowly rotating anisotropic  $\mathcal{C}$ -stars, up to the second order in the angular frequency  $\Omega$ . To this end, we numerically integrated the extended Hartle equations derived in [1], varying central mass density and anisotropy parameter. Our study revealed that, in the limit of high anisotropy and maximum compactness, as constrained by stability, certain rotational perturbations of  $\mathcal{C}$ -stars exhibit a striking similarity to other ultracompact systems. For instance, the constant  $h_c$ , which appears in the monopole sector [see Eq. (26)], approaches the value  $-6J^2/R_S^4$ , coinciding with the result found for ultracompact Schwarzschild stars in the gravastar limit [42], and highly anisotropic Bowers-Liang spheres [1]. These results suggest that this behavior of the constant  $h_c$  may be a generic feature of rotating ultracompact objects. However, further tests on other systems, or possibly a general argument coming from the monopole equations, would be needed to confirm this generality.

Regarding the quadrupole sector, a particularly interesting result is that the ellipticity of the bounding surface changes sign for certain values of anisotropy  $\mathcal{C}$ , beyond certain compactness. Consequently, in these configurations, slow rotation leads to a prolate rather than an oblate shape. Notably, the ellipticity curves remain smooth and well-behaved across the cases considered, in contrast to the Bowers-Liang model where divergences

appeared for specific values of anisotropy and compactness [1]. While the ellipticity transitions to negative values for certain configurations, the reduced quadrupole moment, or Kerr factor, remained positive in all cases studied. Thus, although the surfaces may exhibit negative ellipticity, in certain cases, the overall effect of the quadrupole moment is positive. Finally, we found that for the highly anisotropic case  $\mathcal{C} = 10^4$ , the Kerr factor appears to approach the Kerr BH value, aligning with results from sub-Buchdahl Schwarzschild stars and Bowers-Liang spheres.

The authors in Ref. [29] concluded that  $\mathcal{C}$ -stars may provide a prototypical model for ultracompact objects, since they can be as massive and compact as BHs. While we disagree with this conclusion in the context of the configurations studied in this paper, it is plausible that different choices of the parameters ( $k, \gamma, \mathcal{C}$ ) could yield ultracompact  $\mathcal{C}$ -stars that more closely approach the BH limit. Although this  $\mathcal{C}$ -star may provide a more physically viable model for an anisotropic star (in contrast with the Bowers-Liang model), and allows for relatively high compactness, the configurations we examined remained constrained by stability limits well below the BH limit. Therefore, although we observed some indications of certain rotational properties behaving in a similar fashion to ultracompact systems approaching the BH limit, the evidence remains inconclusive. In principle, other ultra-anisotropic  $\mathcal{C}$ -stars may have limiting compactness very close to the BH value, however, these extremely high values of anisotropy may result in serious numerical instabilities when extended to slow rotation. Thus, identifying other anisotropic systems that support greater compactness, in the stable branch, and examining their behavior under rotation is an area for further investigation.

## VI. ACKNOWLEDGMENTS

We are grateful to John C. Miller for valuable comments and suggestions. C. P acknowledges the support of the Research Centre for Theoretical Physics and Astrophysics, Institute of Physics in Opava, Silesian University in Opava.

### Appendix A: Conditions from the series solutions near the origin

Suppose  $p_r$  can be approximated near  $r = 0$  as a power series

$$p_r = p_0 + p_1 r + p_2 r^2 + p_3 r^3 + \dots \quad (\text{A1})$$

Substituting (A1) into Eq. (58) we obtain

$$\begin{aligned} m = & \frac{4}{3} \pi r^3 \left[ \left( \frac{p_0}{\kappa} \right)^{1/\gamma} + \frac{p_0}{\gamma - 1} \right] \\ & + \pi r^4 \left( \frac{p_1}{\gamma - 1} + \frac{\left( \frac{p_0}{\kappa} \right)^{1/\gamma} p_1}{\gamma p_0} \right) \\ & + \frac{4}{5} \pi r^5 \left[ \frac{p_2}{\gamma - 1} + \frac{\left( \frac{p_0}{\kappa} \right)^{1/\gamma} (p_1^2 - \gamma p_1^2 + 2\gamma p_0 p_2)}{2\gamma^2 p_0^2} \right] + \dots \end{aligned} \quad (\text{A2})$$

Using these expressions for  $p_r$  and  $m$ , Eq. (59) results in a series for which we can equate the coefficients term by term. The lowest order term goes like  $r^{-1}$  and requires

$$\frac{2 \left[ \mathcal{C} \left( n p_0 + \left( \frac{p_0}{\kappa} \right)^{1/\gamma} \right) p_1 \right]}{r} = 0. \quad (\text{A3})$$

To ensure that the pressure does not vanish as we go to the origin, we require  $p_0 \neq 0$ . Consequently, this condition leaves us with two possible options: either  $p_1 = 0$  or  $\mathcal{C} = 0$ .

#### 1. The non-zero anisotropy case: $\mathcal{C} \neq 0$

Suppose we have anisotropy, such that  $\mathcal{C} \neq 0$ . The lowest order term (A3) implies  $p_1 = 0$ , and the next lowest  $r^0$  term gives

$$4\mathcal{C} \left[ n p_0 + \left( \frac{p_0}{\kappa} \right)^{1/\gamma} \right] p_2 = 0. \quad (\text{A4})$$

Thus, we must have  $p_2 = 0$  if anisotropy is present. However, the next linear in  $r$  term gives

$$0 = \left\{ -6\mathcal{C} \left[ n p_0 + \left( \frac{p_0}{\kappa} \right)^{1/\gamma} \right] p_3 - \left[ p_0 + n p_0 + \left( \frac{p_0}{\kappa} \right)^{1/\gamma} \right] \left[ 4\pi p_0 + \frac{4}{3} \pi \left( \left( \frac{p_0}{\kappa} \right)^{1/\gamma} + \frac{p_0}{\gamma - 1} \right) \right] \right\} r,$$

from which we conclude

$$p_3 = -\frac{2\pi \left[ p_0 + np_0 + \left(\frac{p_0}{\kappa}\right)^{1/\gamma} \right] \left[ \left(\frac{p_0}{\kappa}\right)^{1/\gamma} + (3+n)p_0 \right]}{9\mathcal{C} \left[ np_0 + \left(\frac{p_0}{\kappa}\right)^{1/\gamma} \right]}. \quad (\text{A5})$$

Notice that under the reasonable restrictions  $p_0, n, \kappa > 0$ , we find that  $p_3 < 0$  for  $\mathcal{C} > 0$ , and  $p_3 > 0$  for  $\mathcal{C} < 0$ . However, since we have set  $p_1 = p_2 = 0$ , a positive  $p_3$  implies that the lowest-order non-constant behavior in pressure leads to an *increase* as we move away from the origin. This contradicts the expected physical behavior, where pressure should *decrease* outward from the origin.

Numerically, for small negative values of  $\mathcal{C}$ , we find solutions where the pressures remain finite and eventually fall to zero. However, for larger negative magnitudes of  $\mathcal{C}$ , the solutions exhibit divergences, suggesting that the system becomes unstable, or unphysical beyond a certain threshold. In any case, this outward increase in pressure for negative  $\mathcal{C}$  explains why we restrict our analysis to

$\mathcal{C} \geq 0$  throughout the paper <sup>4</sup>.

## 2. Isotropic case: $\mathcal{C} = 0$

Suppose we satisfy Eq. (A3) by considering the isotropic case  $\mathcal{C} = 0$ . The next highest order  $r^0$  term still requires

$$p_1 = 0, \quad (\text{A6})$$

and the  $r^1$  term can be solved to give the constraint

$$p_2 = -\frac{2\pi}{3} \left[ \left(\frac{p_0}{\kappa}\right)^{n/(n+1)} + (n+1)p_0 \right] \times \left[ \left(\frac{p_0}{\kappa}\right)^{\frac{1}{\gamma}} + \frac{p_0}{\gamma-1} + 3p_0 \right]. \quad (\text{A7})$$

Assuming the same reasonable restrictions of  $p_0, n, \kappa > 0$ , this will always be negative. Consequently, the low-order series terms do not indicate any problematic behavior associated with increasing pressure in the isotropic case.

- 
- [1] P. Beltracchi and C. Posada, *Phys. Rev. D* **110**, 024052 (2024), arXiv:2403.08250 [gr-qc].
- [2] J. B. Hartle, *Astrophys. J.* **150**, 1005 (1967).
- [3] J. B. Hartle and K. S. Thorne, *Astrophys. J.* **153**, 807 (1968).
- [4] E. T. Newman and A. I. Janis, *J. Math. Phys.* **6**, 915 (1965).
- [5] E. T. Newman, R. Couch, K. Chinnapared, A. Exton, A. Prakash, and R. Torrence, *J. Math. Phys.* **6**, 918 (1965).
- [6] R. P. Kerr, in *Kerr Fest: Black Holes in Astrophysics, General Relativity and Quantum Gravity* (2007) arXiv:0706.1109 [gr-qc].
- [7] M. Gurses and F. Gursey, *J. Math. Phys.* **16**, 2385 (1975).
- [8] S. P. Drake and P. Szekeres, *Gen. Rel. Grav.* **32**, 445 (2000), arXiv:gr-qc/9807001 [gr-qc].
- [9] M. Azreg-Aïnou, *Phys. Rev. D* **90**, 064041 (2014), arXiv:1405.2569 [gr-qc].
- [10] P. Beltracchi and P. Gondolo, *Phys. Rev. D* **104**, 124066 (2021), arXiv:2104.02255 [gr-qc].
- [11] P. Beltracchi and P. Gondolo, *Phys. Rev. D* **104**, 124067 (2021), arXiv:2108.02841 [gr-qc].
- [12] J. Lense and H. Thirring, *Phys. Z.* **19**, 156 (1918).
- [13] S. Yazadjiev, *Phys. Rev. D* **85**, 044030 (2012), arXiv:1111.3536 [gr-qc].
- [14] J. Frieben and L. Rezzolla, *Mon. Not. Roy. Astron. Soc.* **427**, 3406 (2012), arXiv:1207.4035 [gr-qc].
- [15] V. Folomeev and V. Dzhunushaliev, *Phys. Rev. D* **91**, 044040 (2015), arXiv:1501.06275 [gr-qc].
- [16] R. F. Sawyer, *Phys. Rev. Lett.* **29**, 382 (1972).
- [17] S. L. Liebling and C. Palenzuela, *Living Rev. Rel.* **26**, 1 (2023), arXiv:1202.5809 [gr-qc].
- [18] L. Herrera and N. O. Santos, *Phys. Rept.* **286**, 53 (1997).
- [19] R. L. Bowers and E. P. T. Liang, *Astrophys. J.* **188**, 657 (1974).
- [20] S. S. Bayin, *Phys. Rev. D* **26**, 1262 (1982).
- [21] H. O. Silva, C. F. B. Macedo, E. Berti, and L. C. B. Crispino, *Class. Quant. Grav.* **32**, 145008 (2015), arXiv:1411.6286 [gr-qc].
- [22] K. Yagi and N. Yunes, *Phys. Rev. D* **91**, 123008 (2015), arXiv:1503.02726 [gr-qc].
- [23] B. Biswas and S. Bose, *Phys. Rev. D* **99**, 104002 (2019), [Erratum: *Phys.Rev.D* 111, 029903 (2025)], arXiv:1903.04956 [gr-qc].
- [24] H. C. Das, *Phys. Rev. D* **106**, 103518 (2022), arXiv:2208.12566 [gr-qc].
- [25] M. Cosenza, L. Herrera, M. Esculpi, and L. Witten, *J. Math. Phys.* **22**, 118 (1981).
- [26] D. Horvat, S. Ilijic, and A. Marunovic, *Class. Quant. Grav.* **28**, 025009 (2011), arXiv:1010.0878 [gr-qc].
- [27] L. Herrera, *Phys. Rev. D* **97**, 044010 (2018), arXiv:1801.08358 [gr-qc].
- [28] J. Ovalle, C. Posada, and Z. Stuchlík, *Class. Quant. Grav.* **36**, 205010 (2019), arXiv:1905.12452 [gr-qc].
- [29] G. Raposo, P. Pani, M. Bezares, C. Palenzuela, and V. Cardoso, *Phys. Rev. D* **99**, 104072 (2019), arXiv:1811.07917 [gr-qc].
- [30] A. Alho, J. Natário, P. Pani, and G. Raposo, *Phys. Rev. D* **105**, 044025 (2022), [Erratum: *Phys.Rev.D* 105, 129903 (2022)], arXiv:2107.12272 [gr-qc].
- [31] A. Alho, J. Natário, P. Pani, and G. Raposo, *Phys. Rev. D* **109**, 064037 (2024), arXiv:2306.16584 [gr-qc].
- [32] L. M. Becerra, E. A. Becerra-Vergara, and F. D. Lora-Clavijo, *Phys. Rev. D* **110**, 103004 (2024), arXiv:2410.06316 [gr-qc].

<sup>4</sup> Note that [29] also restricts their analysis to  $\mathcal{C} \geq 0$ , though they do not explicitly discuss the reasoning behind this choice.

- [33] J. C. Miller, *Mon. Not. R. Astron. Soc.* **179**, 483 (1977).
- [34] L. M. Becerra, E. A. Becerra-Vergara, and F. D. Lora-Clavijo, (2025), [arXiv:2504.16305 \[astro-ph.HE\]](#).
- [35] M. L. Pattersons and A. Sulaksono, *Eur. Phys. J. C* **81**, 698 (2021).
- [36] B. Reina and R. Vera, *Class. Quantum Grav.* **32**, 155008 (2015), [arXiv:1412.7083 \[gr-qc\]](#).
- [37] Wolfram Research, Inc., “Mathematica, Version 12.2.0,” Champaign, IL, 2020.
- [38] K. D. Kokkotas and J. Ruoff, *Astron. Astrophys.* **366**, 565 (2001), [arXiv:gr-qc/0011093](#).
- [39] S. L. Shapiro and S. A. Teukolsky, *Black holes, white dwarfs, and neutron stars: The physics of compact objects* (Wiley, 1983).
- [40] R. W. Romani, D. Kandel, A. V. Filippenko, T. G. Brink, and W. Zheng, *Astrophys. J. Lett.* **934**, L17 (2022), [arXiv:2207.05124 \[astro-ph.HE\]](#).
- [41] P. Demorest, T. Pennucci, S. Ransom, M. Roberts, and J. Hessels, *Nature* **467**, 1081 (2010), [arXiv:1010.5788 \[astro-ph.HE\]](#).
- [42] P. Beltracchi and C. Posada, *Class. Quantum Grav.* **41**, 045001 (2024), [arXiv:2305.09544 \[gr-qc\]](#).